

A Unique Combination of Equatorial Plasma Bubble Morphologies Occurring Within a 12 deg Longitude Range

Deepak Kumar Karan¹, Richard W Eastes², Carlos Martinis³, Robert Edward Daniell⁴, Stanley C. Solomon⁵, and William E. McClintock²

¹Laboratory for Atmospheric and Space Physics, University of Colorado

²Laboratory for Atmospheric and Space Physics

³Boston University

⁴Ionospheric Physics Consulting

⁵National Center for Atmospheric Research (UCAR)

December 7, 2022

Abstract

On 12 October 2020, the NASA's Global-scale Observations of the Limb and Disk (GOLD) mission observed three differently shaped EPBs within a 12° longitude range, near the subsatellite point. One is straight aligned to the magnetic field line, whereas the poleward extensions of the others are tilted eastward and westward from the magnetic field line resembling a C-shape and reversed C-shape structures. These EPBs were inside the GOLD imager's field-of-view for a period of ~3 hours. This allowed us to compute their zonal motion and determine their drift velocities. EPBs' drift velocities were derived from measuring their longitudinal shifts at the magnetic equator and at both EIA crests. This unique observation, showing three morphologies in a narrow longitude sector, indicates the occurrence of strong longitudinal gradients in the typical parameters associated with the dynamics of EPBs, like neutral winds, electric fields, or other parameters within such a narrow longitude range.

1 **A Unique Combination of Equatorial Plasma Bubble Morphologies Occurring**
2 **Within a 12° Longitude Range**

3
4 **Deepak Kumar Karan¹, Richard W. Eastes¹, Carlos R. Martinis², Robert E. Daniell³,**
5 **Stanley C. Solomon⁴ and William E. McClintock¹**

6
7 ¹Laboratory for Atmospheric and Space Physics, University of Colorado, Boulder, CO, USA

8 ²Center for Space Physics, Boston University, MA, USA

9 ³Ionospheric Physics, Stoughton, MA, USA

10 ⁴High Altitude Observatory, National Center for Atmospheric Research, Boulder, CO, USA

11
12 Corresponding author: Deepak Kumar Karan (Deepak.Karan@lasp.colorado.edu)

13
14 **Key Points:**

- 15 • First simultaneous observations of C-shape, straight, and reversed C-shape EPBs within
16 12° longitude range
- 17 • Observations indicate longitudinal variations in EPBs' zonal drift velocities at the
18 magnetic equator and EIA crests
- 19 • Different EPBs' shapes in such short longitudes point to small-scale gradients in neutral
20 winds or electric field effects

21
22 **Key Words:** NASA GOLD mission, Equatorial Plasma Bubbles, EPB Morphology, Plasma
23 Irregularities, Nighttime ionosphere, OI 135.6 nm nightglow

32 **Abstract:**

33 On 12 October 2020, the NASA’s Global-scale Observations of the Limb and Disk (GOLD)
34 mission observed three differently shaped EPBs within a 12° longitude range, near the subsatellite
35 point. One is straight aligned to the magnetic field line, whereas the poleward extensions of the
36 others are tilted eastward and westward from the magnetic field line resembling a C-shape and
37 reversed C-shape structures. These EPBs were inside the GOLD imager’s field-of-view for a
38 period of ~3 hours. This allowed us to compute their zonal motion and determine their drift
39 velocities. EPBs’ drift velocities were derived from measuring their longitudinal shifts at the
40 magnetic equator and at both EIA crests. This unique observation, showing three morphologies in
41 a narrow longitude sector, indicates the occurrence of strong longitudinal gradients in the typical
42 parameters associated with the dynamics of EPBs, like neutral winds, electric fields, or other
43 parameters within such a narrow longitude range.

44

45 **Plain Language Summary:**

46 The post-sunset ionosphere becomes conducive to the formation of plasma irregularities that are
47 associated with depleted plasma densities. In the images obtained from space or ground, these
48 plasma depleted regions appear as latitudinally elongated dark bands, which are known as
49 “equatorial plasma bubbles (EPBs)”. The trans-ionospheric radio wave propagation, satellite
50 communication, and navigation systems are adversely affected while the signals travel through the
51 EPBs. Thus, investigations of EPBs’ formation and development are important. On 12 October
52 2020, the NASA’s Global-scale Observations of the Limb and Disk (GOLD) mission observed the
53 three differently shaped EPBs within a 12° longitude range, near the subsatellite point. One is
54 straight aligned to the magnetic field line, whereas the poleward extensions of the others are tilted
55 eastward or westward from the magnetic field line resembling a C-shape or reversed C-shape
56 structure. This is the only observation of this kind so far reported to the best of our knowledge.
57 Such observation indicates the occurrence of strong longitudinal gradients in neutral winds or
58 electric fields. We are presenting detailed information on the observations, obtained their zonal
59 drift velocities at different latitudes, and discussed the possible explanation of their occurrences.

60

61

62

63 **Introduction:**

64 Equatorial plasma bubbles (EPBs), a nighttime plasma irregularity phenomenon, occur within the
65 equatorial and low-latitude ionosphere. Trans-ionospheric radio wave propagation for
66 communication, navigation, and timing is adversely affected when passing through the plasma
67 irregularities in this region. Thus, the investigation of plasma irregularities is an important priority
68 for researchers, with societal implications. The formation and development of EPBs depend on
69 several factors such as vertical and horizontal ionospheric density gradient (both neutral and
70 plasma), background neutral winds, zonal electric fields, chemical recombination, and atmospheric
71 waves (Sultan, 1996; Taori et al., 2011; Liu et al., 2017; Bhattacharyya, 2022). EPBs are expected
72 to be aligned to the magnetic field lines, and in 2-D airglow images, they appear to be straight.
73 However, in different cases, the poleward extensions of the EPBs are observed to be tilted eastward
74 or westward from the magnetic field line resembling either a C-shape or reversed C-shape
75 structures, respectively.

76

77 Using a ground-based all-sky airglow imaging system, westward skewness of the airglow
78 depletions with respect to the magnetic field line away from the magnetic equator was reported
79 (Mendilo and Baumgardner, 1982; Mendilo and Tyler, 1983). A decrease of the eastward plasma
80 drift velocity with increasing altitude (latitude) could be produced if the eastward neutral wind
81 velocity also decreases with altitude (latitude), a direct consequence of a fully working F-region
82 dynamo (Rishbeth, 1972). This latitudinal gradient in the zonal neutral wind has been observed by
83 Dynamics Explorer-2 satellite (Raghavarao et al., 1991) and ground-based Fabry-Perot
84 interferometer (Martinis et al., 2001, 2003). Reversed C-shape EPB was observed in the OI 135.6-
85 nm emission images by the Global Ultraviolet Imager (GUVI) on board the Thermosphere,
86 Ionosphere, Mesosphere Energetics and Dynamics (TIMED) satellite (Kelley et al., 2003). The
87 vertical shear in the eastward plasma flow velocity, which peaks near the F peak at the magnetic
88 equator is attributed to the formation of the EPB structure. Kil et al., (2009) proposed a shell
89 structure to understand this reversed C-shape structure. Several 2-D and 3-D simulation efforts
90 have been put forward in this regard (Huba et al., 2009, 2020; Yokoyama, 2017 and references
91 therein).

92

93 On October 12, 2020, the NASA Global-scale Observations of the Limb and Disk (GOLD)
94 mission observed three EPBs; a C-shape, a straight, and a reversed C-shape EPB occurring within
95 12° of longitude near the subsatellite point (~47° W). Such occurrence of three consecutive
96 different structured EPBs has not been observed before. This paper reports the observations of this
97 rare event with a discussion about the possible causes of its occurrence.

98

99 **Data:**

100 Nighttime OI 135.6 nm partial disk scans made by the GOLD imager are the primary data sets
101 used in this study. The GOLD imager was launched on 25 January 2018 and is located in
102 geostationary orbit at 47.5°W, carried on a commercial communications satellite. Nominal
103 operations and observations started on 9 October 2018. It has two identical spectrographs that
104 obtain images of the Earth in the far-ultraviolet (FUV) range, at ~132-162 nm wavelength. It
105 measures the column integrated emission rate along the line of sight. The night time peak emission
106 altitude for OI 135.6 nm is considered to be at 300 km when geolocating the pixels. GOLD is able
107 to observe the American, Atlantic, and Western African longitudinal regions, which provides a
108 unique opportunity to unambiguously observe the spatial-temporal evolution of various
109 ionospheric-thermospheric features in this active region of the Equatorial Ionization Anomaly
110 (EIA). The night time LIC disk images are obtained at a cadence of 15 minutes and binned to a
111 spatial resolution of 96×80 km at the nadir. Detailed information about the GOLD instrument,
112 observation mode, and data products with some initial observations are discussed in Eastes et al.,
113 (2017, 2020) and McClintock et al., (2020).

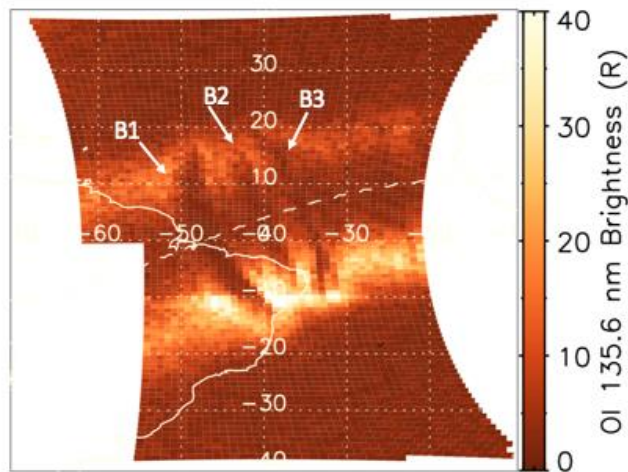
114

115

116 **Results and Discussion:**

117 GOLD takes nighttime disk observations using both channels A and B (CHA and CHB hereafter).
118 Most individual scans cover ~45° in longitude, ~3 hours in local time, just east of the sunset
119 terminator. Starting from 20:10 UT, CHB takes the night time partial disk images alternating
120 between the Northern and Southern hemispheres. Simultaneous observations from the Northern
121 and Southern hemispheres are made from 23:10 to 00:09 UT, using CHA and CHB. The
122 observation sequence is described in detail by Karan, et al. (2020). On 12 October 2020 GOLD
123 measured three closely spaced EPBs during 23:10 and 23:55 UT. Figure 1 shows simultaneous

2020_286_23_10



124

Figure 1. The nighttime images obtained by GOLD in OI 135.6 nm simultaneously by CHA and CHB at 23:10 UT on 12 October 2020 are combined. The white dashed line shows the geomagnetic equator. The two bright emission patches seen at all longitudes on either side of the magnetic equator are the EIA crests. Depletions in the brightness across the EIA crests, known as Equatorial Plasma Bubbles (EPBs), are seen. The C-shape, straight, and reversed C-shape EPBs are noted as B1, B2, and B3, respectively.

125 images obtained by CHA and CHB from the northern and southern hemispheres at 23:10 UT. The
126 white dashed line shows the geomagnetic equator. The observed bright emissions on either side of
127 the geomagnetic equator are the EIA crests. The horizontal glitch in brightness at 10°S GLat is a
128 data artifact due to the high voltage being too low during the flat field measurements, which is
129 explained in section 3.1.18 of the GOLD data release note Rev 4.6 ([https://gold.cs.ucf.edu/wp-](https://gold.cs.ucf.edu/wp-content/documentation/GOLD_Release_Notes_Rev4.6.pdf)
130 [content/documentation/GOLD_Release_Notes_Rev4.6.pdf](https://gold.cs.ucf.edu/wp-content/documentation/GOLD_Release_Notes_Rev4.6.pdf)). Depletions in the brightness across
131 the EIA crests are identified as EPBs. Three clear and distinct EPBs over the Eastern side of South
132 America are observed in this image. The EPB on the left side (marked as B1) has a C-shape
133 structure, the one in the middle (marked as B2) is almost straight, whereas the right EPB (marked
134 as B3) has a reversed C-shape structure. Each type of EPB structure has been observed in the past,
135 but the observations on October 12, 2020, represent a rare event where the three different types of
136 EPBs occur consecutively over a narrow longitude range ($\sim 12^\circ$) between $\sim 47^\circ$ W and 35.5° W.
137 This longitude range is close to the crossing longitude of geographic and geomagnetic equators,
138 and also near to the subsatellite location of the GOLD imager.

139

140

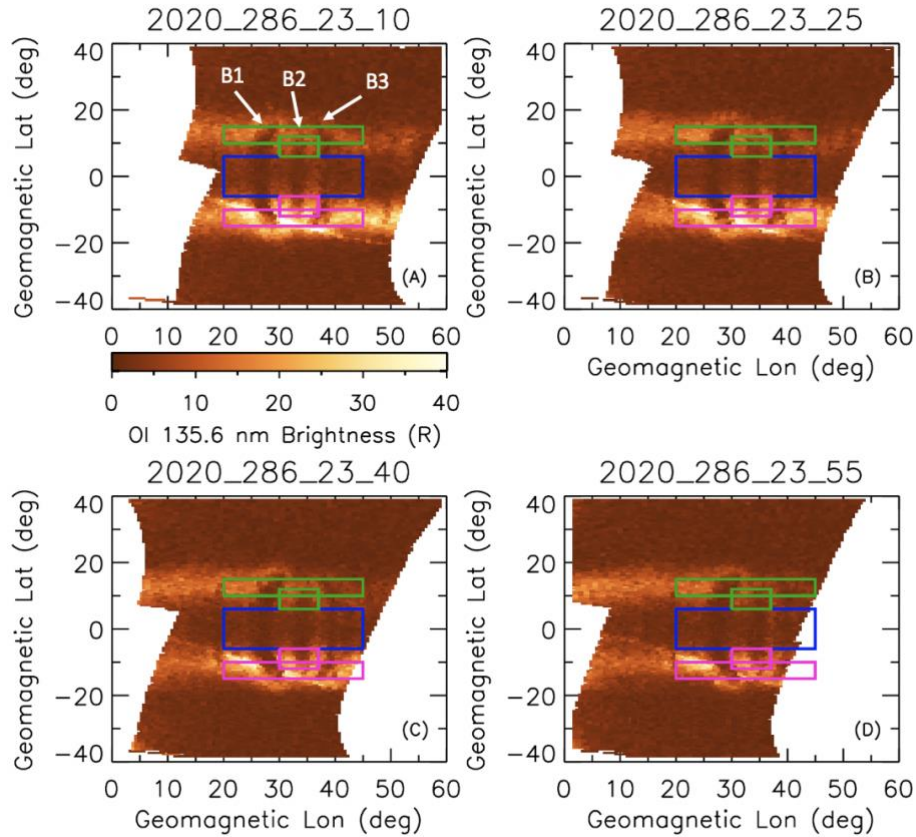
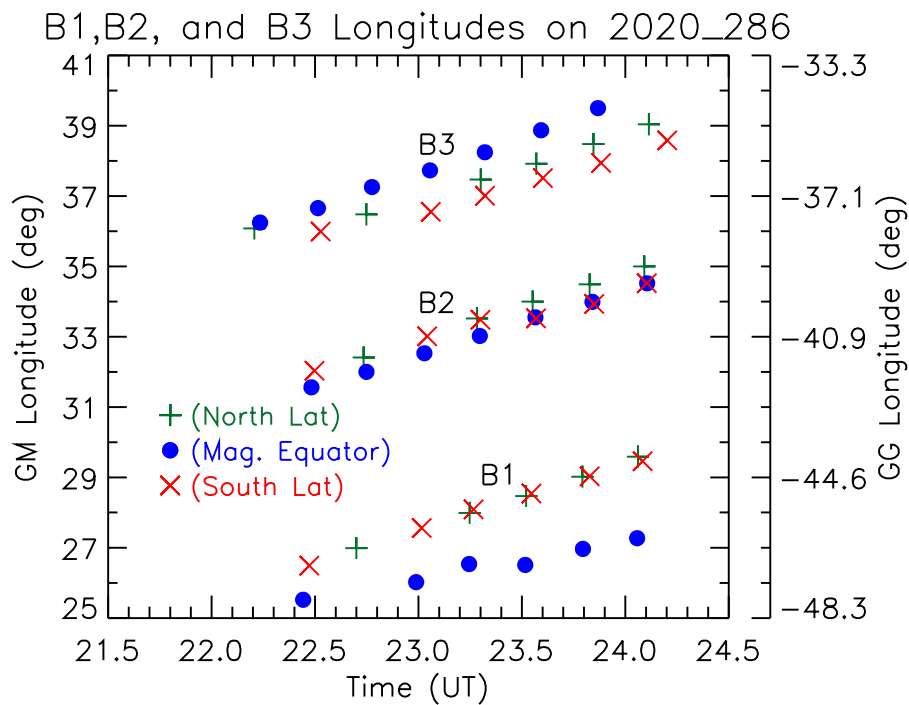


Figure 2. (A, B, C, and D) show the nighttime images observed by GOLD at 23:10, 23:25, 23:40, and 23:55 UT, respectively in geomagnetic co-ordinates. The green, blue, and magenta boxes are the regions selected at the N- crest, magnetic equator, and S- crest of EIA latitudes (common on each panel).

141

142 In order to investigate the different shapes of these EPBs within the narrow longitude range in
 143 detail, we transformed the EPBs from geographic coordinates into QD dipolar magnetic co-
 144 ordinates (Laundal and Richmond, 2017; Thébault et al., 2015). Figures 2 (A), (B), (C), and (D)
 145 show the nighttime images observed by GOLD at 23:10, 23:25, 23:40, and 23:55 UT, respectively
 146 in magnetic coordinates. At 23:10 UT (Figure 2A) the locations of B1, B2, and B3 at the magnetic
 147 equator are (47° W Glon, 0.5° N Glat, 26.5° Mlon), (40° W Glon, 2.5° N Glat, 33.2° Mlon), and
 148 (35.5° W Glon, 5.7° N Glat, 38.5° Mlon), respectively. We next investigated their zonal motion (or
 149 shifts) at different magnetic latitude ranges. We selected three magnetic latitude regions, (10° to
 150 15°), (-6° to 6°), and (-15° to -10°), shown by green, blue, and magenta boxes, respectively, in
 151 Figure 2. The latitude ranges are selected to distinguish both the EIA crests from the magnetic
 152 equatorial region. The green and magenta boxes cover the N and S EIA crests latitudes. The blue

153 boxes cover the magnetic equatorial latitudes. We note that B2 reaches lower latitudes than B1
 154 and B3. So, for B2 the selected magnetic latitude ranges at EIA crests are (6° to 12°) and (-12° to
 155 -6°). The brightness along the latitudes in each box are summed at each longitude. From the
 156 longitudinal variations of the summed brightness, the longitudes of the EPBs are obtained. This
 157 method of obtaining the EPB location is explained in detail by Karan et al., 2020. Longitudes of
 158 B1, B2, and B3 at the three latitude ranges are obtained from the partial disk images covering the
 159 EPBs on October 12, 2020. The obtained EPB locations at the different latitude ranges are shown
 160 in Figure 3.
 161



162 Figure 3 shows EPB (B1, B2, and B3) longitudes at different times of observations. Blue
 163 dot, green plus, and red cross symbols indicate to longitudes as obtained at the magnetic
 164 equator, N and S EIA crests latitudes, respectively.

163 Longitudes of each EPB are obtained at the magnetic equator, N and S EIA crests latitudes, which
 164 are shown by blue dots, green plus, and red cross symbols, respectively in figure 3. The EPB
 165 locations are obtained multiple times, one of the advantages of the GOLD observations. Earlier
 166 detection of B3 at 22:10 UT is due to the GOLD imager's observation sequence from east to west
 167 following the sunset terminator. EPBs are developed at the geomagnetic equator and grow to
 168

169 higher altitudes and latitudes. Thus, EPBs are detected first closer to equatorial latitudes. One
 170 common pattern observed is that three EPBs shift to east longitudes with time at each latitude
 171 range. From the temporal shifts of the locations, EPB drift velocities can be derived. Using the
 172 method discussed in Karan et al. (2020), drift velocities of B1, B2, and B3 are obtained at the three
 173 latitude ranges and are listed in the table.

Magnetic Latitude Zone	B1 (C-shape)	B2 (Straight)	B3 (reversed C-shape)
N-EIA crest	65 ± 2	62 ± 4	57 ± 9
Equator	48 ± 6	62 ± 2	68 ± 4
S-EIA crest	62 ± 3	61 ± 5	52 ± 5

Table 1. Zonal drift velocities (m/s) of B1, B2, and B3 at the magnetic equator, N and S EIA crest latitudes

174

175

176 The drift velocities of B1 are 65 ± 2 , 48 ± 6 , and 62 ± 3 m/s at the N crest, magnetic equator, and
 177 S crest, respectively. At the EIA crest latitudes, B1 was drifting faster than at the equator. This can
 178 explain its C-shape structure. B2 was drifting at a constant velocity of ~ 62 m/s at all the latitude
 179 ranges. As a result, it had a straight shape, not showing any latitudinal variation. The drift velocities
 180 of B3 are 57 ± 9 , 68 ± 4 , and 52 ± 5 m/s at the N crest, magnetic equator, and S crest, respectively.
 181 B3 was drifting faster near the magnetic equator than at the EIA crest latitudes. This resulted in
 182 the reversed C-shape B3. The obtained EPB drift velocities explain the observed different EPB
 183 structures.

184

185 All these differences were observed in a short longitude range of ~ 12 degrees. As explained earlier,
 186 the behavior of zonal winds affects the motion of plasma drifts, thus we can interpret the shapes
 187 observed as a consequence of the varying conditions on the thermospheric neutral winds at these
 188 longitudes. Geomagnetic conditions were quiet during this time, so we can exclude any storm
 189 effects. We would expect larger ion drag forces to reduce the neutral zonal wind speeds at the EIA
 190 crests, allowing faster winds at the magnetic equator. As a result, EPB zonal drift velocity would
 191 be reduced at these crest latitudes (Raghavarao et al., 1991; Martinis et al., 2001, 2003; Valladares
 192 et al., 2002) and a reversed C-shape structure would be formed. This is the case with B3. Since B2
 193 did not evolve to latitudes reaching the peak of the EIA crests, ion drag effects might not be too

194 different at the N and S crests when compared to the magnetic equator. As a consequence, the
195 EPB drift velocities observed would be similar, and no latitudinal variation in the shape of B2 is
196 observed. However, the ion drag force mechanism does not explain the formation of the C-shape
197 EPB B1 where the drift velocities at the EIA crests are faster than at the equator. A way to reduce
198 a thermospheric neutral wind is through the presence of significant E region contribution to
199 ionization. That would preclude a full F region dynamo operating at the equatorial and low
200 latitudes. As a consequence, the drifts would be slower when compared to the ones observed at
201 higher latitudes, near the peak of the EIA crests, where E-region effects would not be as strong.
202 Thus, while we expect ion drag still affect the overall motion of plasma, E region effects are
203 stronger at the magnetic equator. In fact, from Table 1 we can see that the drifts at the magnetic
204 equator are smallest for B1. Small spatial scale variations ($\sim 3^\circ$ longitude) in the equatorial electric
205 fields have been reported by Karan and Pallamraju (2017).

206

207 **Conclusions:**

208 We have reported a rare occurrence of the EPB morphology using the NASA's GOLD mission
209 observations. Three consecutive EPBs with C-shape, straight, and reversed C-shape structures are
210 observed within a 12° longitude range over the eastern side of South America on October 12, 2020.
211 The longitude of observation of this event is close to the crossing of geographic and geomagnetic
212 equators and also, close to the subsatellite point of the GOLD imager. The drift velocities of B1,
213 B2, and B3 at three latitudes are given in Table 1. Latitudinal variations in drift velocities can
214 explain the difference EPBs' shapes. Different EPBs' shapes in such short longitude range point
215 to small scale gradients in neutral winds or E-region effects at earlier local times.

216

217 **Acknowledgements:**

218 This research is supported by NASA contract 80GSFC18C0061 to the University of Colorado.

219

220 **Open Research:**

221 The GOLD L1C nighttime partial disk data presented in this paper (Level 1C – NI1) can be
222 accessed at the GOLD Science Data Center (<http://gold.cs.ucf.edu/search/>). Please be sure to read
223 the GOLD data release note Rev 4.6 ([https://gold.cs.ucf.edu/wp-](https://gold.cs.ucf.edu/wp-content/documentation/GOLD_Release_Notes_Rev4.6.pdf)
224 [content/documentation/GOLD_Release_Notes_Rev4.6.pdf](https://gold.cs.ucf.edu/wp-content/documentation/GOLD_Release_Notes_Rev4.6.pdf)).

225 **Reference:**

226 Bhattacharyya, A. (2022). Equatorial Plasma Bubbles: A Review. *Atmosphere* 2022, 13, 1637.
227 <https://doi.org/10.3390/atmos13101637>

228

229 Eastes, R. W., McClintock, W. E., Burns, A. G., Anderson, D. N., Andersson, L., Codrescu, M.,
230 et al. (2017). The Global-scale Observations of the Limb and Disk (GOLD) mission. *Space Sci*
231 *Rev*, 212, 383, doi:10.1007/s11214-017-0392-2

232

233 Eastes, R. W., McClintock, W. E., Burns, A. G., Anderson, D. N., Andersson, L., Aryal, S., et al.
234 (2020). Initial observations by the GOLD mission. *J. Geophys. Res. Space Physics*, 125,
235 e2020JA027823, doi:10.1029/2020JA027823

236

237 Huba, J. D., S. L. Ossakow, G. Joyce, J. Krall, and S. L. England (2009), Three-dimensional
238 equatorial spread F modeling: Zonal neutral wind effects, *Geophys. Res. Lett.*, 36, L19106,
239 doi:10.1029/2009GL040284.

240

241 Huba, J. D., & Liu, H.-L. (2020). Global modeling of equatorial spread F with
242 SAMI3/WACCM-X. *Geophysical Research Letters*, 47, e2020GL088258.
243 <https://doi.org/10.1029/2020GL088258>

244

245 Karan, D. K., and D. Pallamraju, (2017). Small-scale longitudinal variations in the daytime
246 equatorial thermospheric wave dynamics as inferred from oxygen dayglow emissions. *J.*
247 *Geophys. Res. Space Physics*, 122, 6528-6542, doi:10.1002/2017JA023891

248

249 Karan, D. K., Daniell, R. E., England, S. L., Martinis, C. R., Eastes, R. W., Burns, A. G., &
250 McClintock, W. E. (2020). First zonal drift velocity measurement of equatorial plasma bubbles
251 (EPBs) from a geostationary orbit using GOLD data. *J. Geophys. Res. Space Physics*, 125,
252 e2020JA028173, doi:10.1029/2020JA028173

253

254 Kelley, M. C., Makela, J. J., Paxton, L. J., Kamalabadi, F., Comberiate, J. M., and Kil, H. (2003),
255 The first coordinated ground- and space-based optical observations of equatorial plasma bubbles,
256 *Geophys. Res. Lett.*, 30, 1766, doi:10.1029/2003GL017301, 14.
257

258 Kil, H., R. A. Heelis, L. J. Paxton, and S.-J. Oh (2009), Formation of a plasma depletion shell in
259 the equatorial ionosphere, *J. Geophys. Res.*, 114, A11302, doi:10.1029/2009JA014369.
260

261 Laundal, K. M., and Richmond, A. D. (2017) Magnetic Coordinate Systems, *Space Sci Rev*, 206,
262 27-59. <https://doi.org/10.1007/s11214-016-0275-y>
263

264 Liu, H., N. Pedatella, and K. Hocke (2017), Medium-scale gravity wave activity in the
265 bottomside F region in tropical regions, *Geophys. Res. Lett.*, 44, 7099–7105,
266 doi:10.1002/2017GL073855.
267

268 Martinis, C., J. Meriwether, M. Biondi, R. Niciejewski, C. Fesen, and M. Mendillo (2001),
269 Zonal neutral winds at equatorial and low-latitudes, *J. Atmos. Sol. Terr. Phys.*, 63, 1559–1569.
270

271 Martinis, C., Eccles, J. V., Baumgardner, J., Manzano, J., & Mendillo, M. (2003). Latitude
272 dependence of zonal plasma drifts obtained from dual-site airglow observations. *Journal of*
273 *Geophysical Research*, 108(A3), 1129. <https://doi.org/10.1029/2002JA009462>
274

275 McClintock, W. E., Eastes, R. W., Beland, S., Bryant, K. B., Burns, A. G., Correia, J., et al
276 (2020). Global-scale Measurements of the Limb and Disk (GOLD) Mission Implementation: 2.
277 Observations, Data Pipeline and Level 1 Data Products. *Journal of Geophysical Research: Space*
278 *Physics*, 125, e2020JA027809. <https://doi.org/10.1029/2020JA027809>.
279

280 Raghavarao, R., L. E. Wharton, N. W. Spencer, H. G. Mayr, and L. H. Brace (1991), An
281 equatorial temperature and wind anomaly (ETWA), *Geophys. Res. Lett.*, 18 (7), 1193–1196,
282 doi:10.1029/91GL01561.
283

284 Richmond, A. D. (1995), Ionospheric electrodynamics using magnetic apex coordinates, J.
285 Geomagn. Geoelectr., 47, 191–212, <https://doi.org/10.5636/jgg.47.191>.
286

287 Rishbeth, H (1972), Thermospheric winds and the F-region: A review, Journal of Atmospheric
288 and Terrestrial Physics, 34, [https://doi.org/10.1016/0021-9169\(72\)90003-7](https://doi.org/10.1016/0021-9169(72)90003-7).
289

290 Sultan, P. J. (1996), Linear theory and modeling of the Rayleigh-Taylor instability leading to the
291 occurrence of equatorial spread F, J. Geophys. Res., 101(A12), 26875– 26891,
292 doi:10.1029/96JA00682.
293

294 Taori, A., A. K. Patra, and L. M. Joshi (2011), Gravity wave seeding of equatorial plasma
295 bubbles: An investigation with simultaneous F region, E region, and middle atmospheric
296 measurements, J. Geophys. Res., 116, A05310, doi:10.1029/2010JA016229.
297

298 Thébault, E., Finlay, C.C., Beggan, C.D. et al. (2015), International Geomagnetic Reference
299 Field: the 12th generation. Earth Planet Sp 67, 79, doi:10.1186/s40623-015-0228-9.
300

301 Tsunoda, R. T., R. C. Livingston, and C. L. Rino (1981), Evidence of a velocity shear in bulk
302 plasma motion associated with the post-sunset rise of the equatorial F layer, Geophys. Res. Lett.,
303 8, 807–810, doi:10.1029/GL008i007p00807.
304

305 Valladares, C. E., J. W. Meriwether, R. Sheehan, and M. A. Biondi, Correlative study of neutral
306 winds and scintillation drifts measured near the magnetic equator, J. Geophys. Res., 107(A7),
307 1112, doi:10.1029/2001JA000042, 2002.
308

309 Yokoyama, T. A review on the numerical simulation of equatorial plasma bubbles toward
310 scintillation evaluation and forecasting. Prog Earth Planet Sci 4, 37 (2017).
311 <https://doi.org/10.1186/s40645-017-0153-6>